**Floquet Analysis.** Our kicked top Hamiltonian is periodic in time, $H(t+\tau) = H(t)$, and for the form given in Eq. (1), with f being a δ-function, the Floquet operator (unitary time-propagator for one full period of $H(t)$) is

$$U = e^{-ipF_y} e^{-i(\kappa/2F)F_x^2} \, .$$

In our experiment, the Floquet operator is slightly modified by the use of finite-duration magnetic field pulses and the application of small bias magnetic fields (see next section), but can readily be determined by numerical integration of the Schrödinger equation. Solving the eigenvalue equation for the Floquet operator,

$$U|e_n\rangle = e^{-i\Phi_n}|e_n\rangle,$$

yields the eigenstates $|e_n\rangle$ (the Floquet states) and the Floquet eigenphases Φ_n. The Floquet states form a convenient basis in which to analyze and understand the quantum dynamics[1]. Supplementary Fig. 1 shows the Husimi distributions of the seven Floquet states for the Hamiltonian used in our experiment. Comparing to the classical phase space plot (Fig. 1), one sees immediately that states $|e_1\rangle$ and $|e_2\rangle$ overlap with the large regular island in the $F_y < 0$ hemisphere, the states $|e_3\rangle$ and $|e_4\rangle$ overlap mostly with the pair of regular islands in the $F_y > 0$ hemisphere, and the remaining states overlap mostly with the chaotic sea. The eigenphases associated with these states are given in Supplementary Table 1, along with the Floquet state populations, $p_n = |\langle e_n|\psi_i\rangle|^2$, for each of the three initial states used in Fig. 2C.
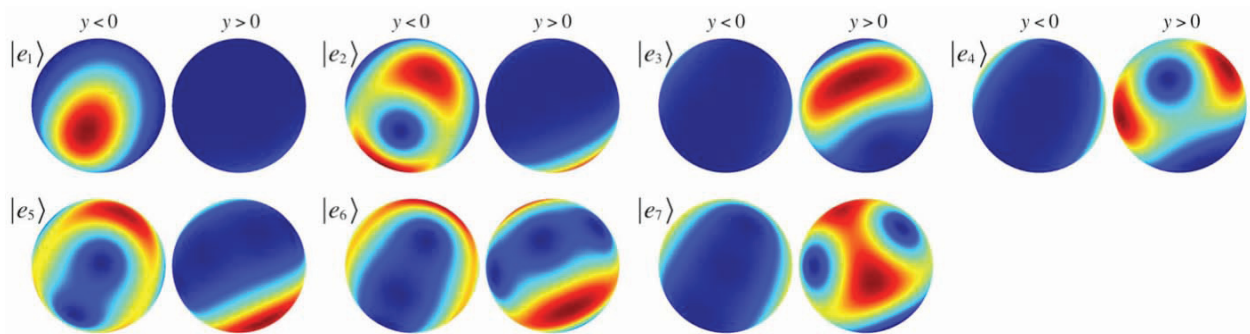
Supplementary Figure 1 | Floquet Eigenstates. Quantum phase space (Husimi) distributions for the seven eigenstates of the Floquet operator, for the experimental conditions of Fig. 2.

Floquet States	Eigenphase	p_n (large island, Fig. 2C, c)	p_n (island pair, Fig. 2C, a)	p_n (chaos, Fig. 2C, b)
$|e_1\rangle$	-2.7738	0.86	0.00	0.02
$|e_2\rangle$	-1.0155	0.10	0.00	0.08
$|e_3\rangle$	-2.1960	0.00	0.41	0.17
$|e_4\rangle$	-2.4308	0.00	0.51	0.09
$|e_5\rangle$	0.5174	0.02	0.01	0.18
$|e_6\rangle$	1.8317	0.02	0.03	0.25
$|e_7\rangle$	2.8812	0.00	0.04	0.21

Supplementary Table 1 | Floquet decomposition of initial states of Fig. 2. Overlap of the three initial states of Fig. 2C with each of the seven eigenstates of the Floquet operator.

   The stroboscopic dynamics can now be interpreted in terms of the Floquet states and eigenphases. The initial state centered on the $F_y < 0$ island is almost entirely supported on the single Floquet state $|e_1\rangle$, is therefore close to an eigenstate of the Floquet operator, and remains almost unchanged between the beginning of one period and the next. In contrast, the initial state centered on one of the islands of the $F_y > 0$ pair is very close to an equal superposition of two Floquet states $|e_3\rangle$ and $|e_4\rangle$. Dynamical tunneling occurs because the Floquet eigenphases are different, causing the relative phase in the superposition to advance by $\Delta\Phi = \Phi_3 - \Phi_4 = 0.2348$ between the beginning of one period and the next. Thus, after $\pi/\Delta\Phi = 13.4$ periods the state has tunneled from one island to the other, and after $2\pi/\Delta\Phi = 26.8$ periods it has returned to the starting point. This simple analysis does not account for decoherence or inhomogeneity in κ, but nevertheless predicts a tunneling period that is in good quantitative agreement with the experimental observation in Fig. 2A. Finally, the initial state centered in the chaotic sea has significant support on four states with eigenphases whose differences are incommensurate. As a result this state evolves in a complex and non-periodic fashion, as evidenced by the experimental observation in Fig. 2B.

Details of the Kicked top implementation. In our experiment, the twisting part of the Kicked Top Hamiltonian is derived from the interaction between an atom and a monochromatic laser field. For a laser polarization along the x-axis, the AC Stark shift (light shift) of a ground hyperfine manifold of given F takes the form $\hbar\xi F_x^2 = \beta\hbar\gamma_s F_x^2$, where γ_s is the rate of spontaneous photon scattering[2]. The dimensionless parameter β depends on the atomic structure and the frequency of the laser field, and is a measure of the relative timescales for coherent evolution and the decoherence caused by scattering. For the $F = 3$ manifold of a Cs atom and a laser field tuned in-between the $6S_{1/2}(F = 3) \rightarrow 6P_{1/2}(F' = 3,4)$ components of the D1 transition, we obtain a maximum value of $\beta \approx 5$, the best available for any alkali atom. Comparing to Eq. 1, it follows that the average number of photon scattering events per Kicked Top period τ is $\gamma_s\tau = \kappa/2\beta F \approx 1/15$, for $\kappa = 2$. Because it takes a few photon scattering events to randomize an $F = 3$ spin state, this allows us to observe mostly coherent dynamics over a few tens of kicks.

   We choose the characteristic parameters p, κ for our Kicked Top based on two main considerations. First, the classical phase space must have regions of regular as well as chaotic motion that are large enough to accommodate most of the Husimi distribution for a minimum uncertainty spin-coherent state. This is essential if we are to associate initial states with one type of dynamics or the other. We have numerically integrated the classical equations of motion, and obtained stroboscopic phase space plots for a broad range of p, κ. Judging from these plots, and keeping in mind that κ should be kept as small as possible to minimize decoherence, we find that values of $p = \pi/4 + 0.2 \approx 0.99$ and $\kappa = 2.0$ produce a suitable mixed phase space. The second consideration is that the Kicked Top dynamics, at least in regular regions, must be robust enough that it can be reliably reproduced and is not washed out by perturbations that vary inhomogeneously across the ensemble. In our setup, the most important perturbation is the 5% variation in κ due to laser beam inhomogeneity. Uncompensated background AC magnetic fields, which average $\sim 50\,\mu G$ RMS for each coordinate axis and fluctuate slightly from day to day, also pose a significant challenge. Fortunately, a workaround for the latter problem can be found by studying the effect of small DC magnetic fields on dynamical tunneling. We have found empirically, both through examination of the Floquet eigenphases and through simulation of the dynamical evolution, that the effect of a DC magnetic field applied along the z-axis is equivalent to reducing the barrier height for a particle tunneling in a double-well potential. Similarly, a DC magnetic field along the x-axis is equivalent to the introduction of an energy asymmetry in a double-well. For our parameters the tunneling period is $\sim 41\tau$ in the absence of background fields. Adding a DC field of as little as $\sim 150\,\mu G$ along the x-axis reduces the amplitude of the tunneling oscillations almost to zero, which suggests that the dynamics may not be robust enough to tolerate our background fields. However, a DC bias of $2\,mG$ along the z-axis will reduce the tunneling period to $\sim 27\tau$, and suppress the sensitivity to fields in the x-direction by more than a factor of two. In practice, we have found that this bias field is essential, and that it allowed us to observe reproducible, coherent tunneling with a period that matches the theoretical prediction. It was therefore present in every experiment and included in all theoretical modeling, including the stroboscopic phase space plot of Fig. 1, the average Husimi distributions of Fig. 2C, and the Floquet analysis outlined above. It must be emphasized that the bias field only serves to improve the robustness of the dynamics, and that it does not alter the structure of the Floquet states or the classical phase space in any significant way.

Numerical Modeling. We model the evolution of our quantum kicked top in two ways. The first and simplest approach is based on numerical integration of the Schrödinger equation, starting from a spin coherent state $|\theta,\phi\rangle$, and using the kicked top Hamiltonian of Eq. (1) with our nominal values for the parameters κ and p. The time evolved state can subsequently be used to compute such quantities as the linear entropy for the electron spin, as done in Fig. 4. This type of model serves as a useful baseline by predicting the outcome of an ideal, perturbation free experiment without decoherence or κ uncertainty.

A more realistic approach is to model the interaction of a ^{133}Cs atom in the $F = 3$ hyperfine ground state with a laser field tuned near the D1 resonance line. This is accomplished by solving a master equation of the standard Lindblad form,

$$\frac{d\rho}{dt} = \frac{i}{\hbar}[H,\rho] + \sum_q \left[D_q \rho D_q^\dagger - \frac{1}{2}\left\{ D_q^\dagger D_q, \rho \right\} \right],$$

with $H = H_A + H_{AL}$, where H_A is the unperturbed atomic Hamiltonian and H_{AL} is the Hamiltonian for the electric dipole interaction between the atom and the laser field,

$$H_{AL} = -\frac{1}{2}\left[\mathbf{E} \cdot \mathbf{d}_{ge} + \mathbf{E}^* \cdot \mathbf{d}_{eg} \right].$$

Here, $\mathbf{E}$ is the complex electric field, and $\mathbf{d}_{ge} = \mathbf{d}_{ge}^\dagger = P_g \mathbf{d} P_e$ is the electric dipole operator, where P_g and P_e are the projectors onto the ground and excited state manifolds. The Lindblad terms correspond to spontaneous emission events described by the jump operators $D_q = \boldsymbol{\varepsilon}_q \cdot \mathbf{d}_{ge}$. For our off-resonant laser field the ground state variables evolve much more slowly than excited state variables, and the latter can be adiabatically eliminated to obtain an effective master equation that involves only populations and coherences in the $F = 3$ manifold[3,4]. At this point a magnetic dipole interaction $g_F \mu_B \mathbf{B}(t) \cdot \mathbf{F}$ can be included, and the effective atom-laser interaction cast in terms of its irreducible rank-2 tensor component, $H_{AL} = \hbar \xi F_x^2$. This leaves us with an overall ground state Hamiltonian of the form given in Eq. (1). To account for κ variation in the experiment, we numerically solve the master equation for a given initial state and a range of κ, and then obtain the density operator by performing a statistical average over the probability distribution $p(\kappa)$. The time evolved density matrix can subsequently be used to calculate Husimi distributions and other quantities for quantitative comparison with experimental data, as was done in Figs. 3 and 4B.

It is important to note that the master equation approach outlined above is an integral part of our protocol for quantum state reconstruction, and that its ability to accurately model our atomic spin system has been well established in previous work[5,6]. Successful quantum state reconstruction requires independent measurements to precisely calibrate the applied magnetic fields, and to determine the first three moments (mean, standard deviation and skew) of the distribution $p(\kappa)$ [7]. These measurements also serve to determine the parameters κ and p that characterize our kicked top dynamics. The only remaining input for our model is the initial state, which we estimate by performing a single Stern-Gerlach measurement of the magnetic sublevel populations in the $F = 3$ ground manifold[8]. This estimate is updated on a regular basis, and the most recent one used in the model. As a result, there are no free parameters or data fitting involved in any of the theory predictions shown in this work.

Stop-motion movies of spin dynamics. Due to page limitations, Fig. 2 shows only a subset of representative frames of the 40-period dynamical evolution of two initial states. Supplementary Figures 2, 3 and 4 show the entire set of frames from a stop-motion movie of a third initial state centered on the large regular island in the $F_y < 0$ hemisphere, as well as the entire set of frames from the stop-motion movies of Fig. 2. These data sets can also be viewed in movie form in Supplementary Videos 1(a), 2(a) and 3(a). For comparison, theoretical simulations based on our full Master Equation model can be seen in movie form in Supplementary Videos 1(b), 2(b) and 3(b).
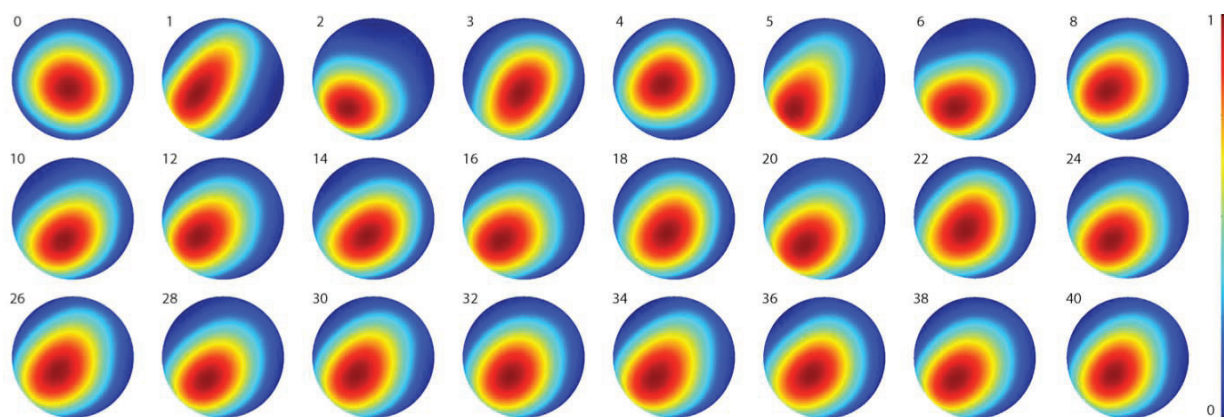
Supplementary Figure 2 | Large Regular Island. Evolving quantum phase space (Husimi) distributions for an initial state centered on the large island in the $F_y < 0$ hemisphere. The period number is indicated to the upper left of each frame. This sequence contains our entire experimental data set, as used in the average shown in Fig. 2C, c. The Husimi distributions are almost entirely confined to the $F_y < 0$ hemisphere, which is therefore the only one shown here.
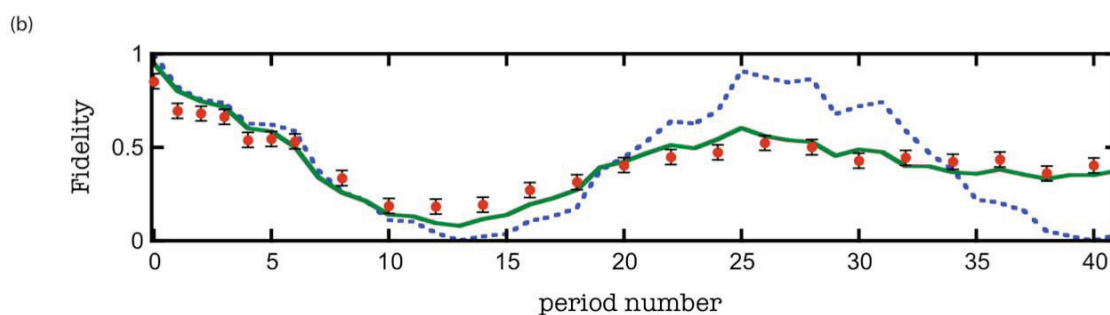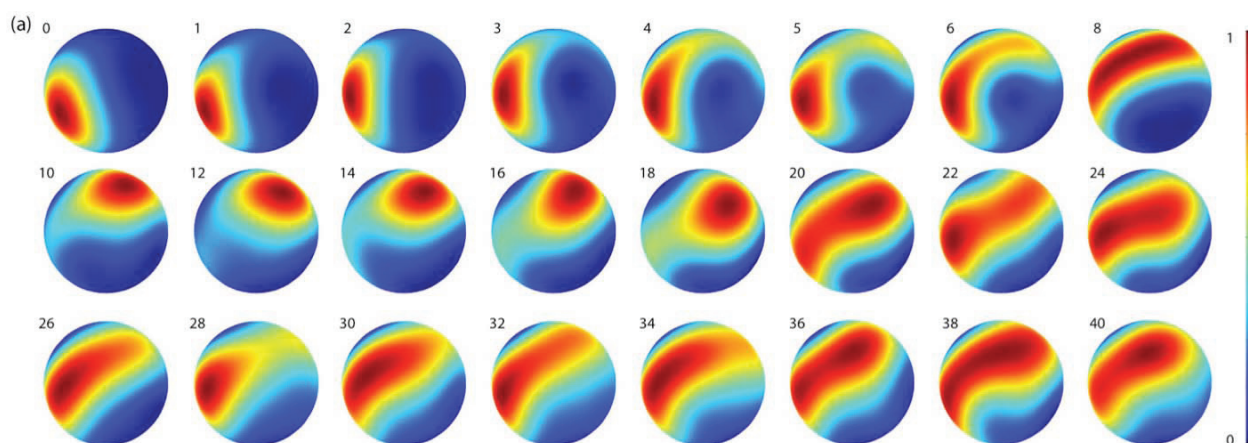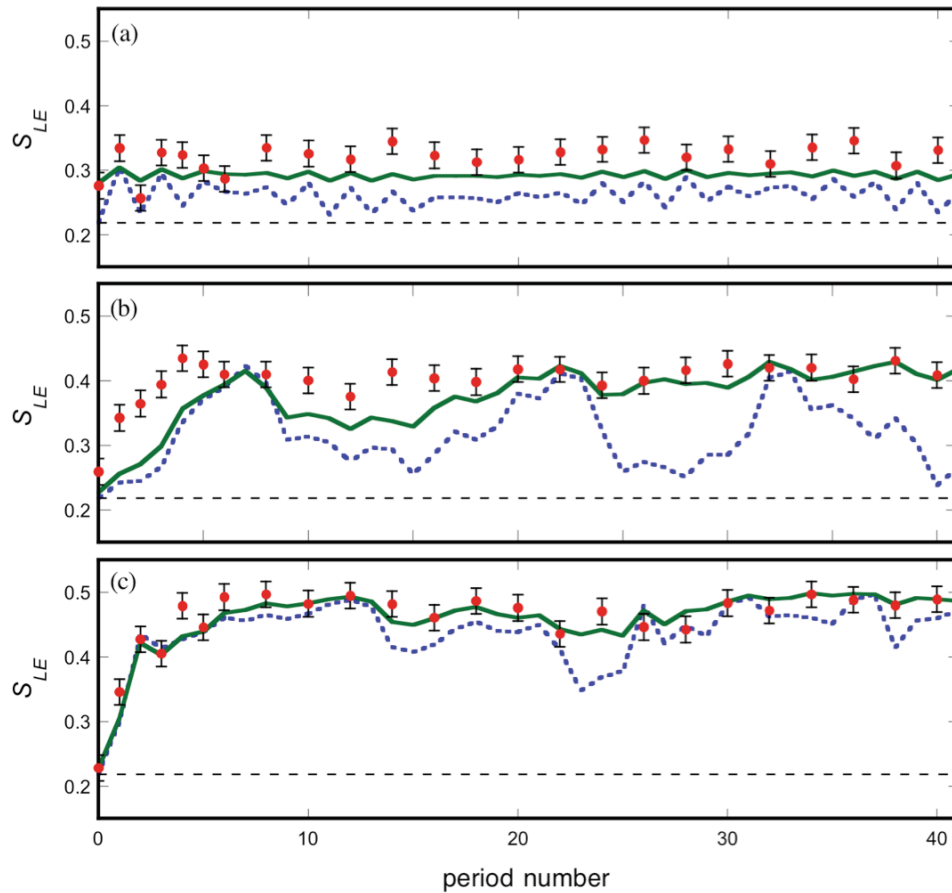

Supplementary Figure 3 | Dynamical Tunneling. (a) Evolving quantum phase space (Husimi) distributions for an initial state centered on the lower of the pair of islands in the $F_y > 0$ hemisphere. The period number is indicated to the upper left of each frame. This sequence contains our entire experimental data set, as used in the average shown in Fig. 2C, a, including the frames missing from Fig. 2A. The Husimi distributions are almost entirely confined to the $F_y > 0$ hemisphere, which is therefore the only one shown here. (b) Fidelity $\mathcal{F} = [Tr\sqrt{\rho_0^{1/2}\rho_n\rho_0^{1/2}}]^2$ between the initial state ρ_0 and the state ρ_n as a function of the period number n. Red dots are experimental data, the dashed blue line is the prediction from a perturbation free model based on the Schrödinger equation, and the solid green line is the prediction from our full Master Equation model including decoherence from light scattering and variations in κ. Experimental error bars are plus/minus one standard deviation.
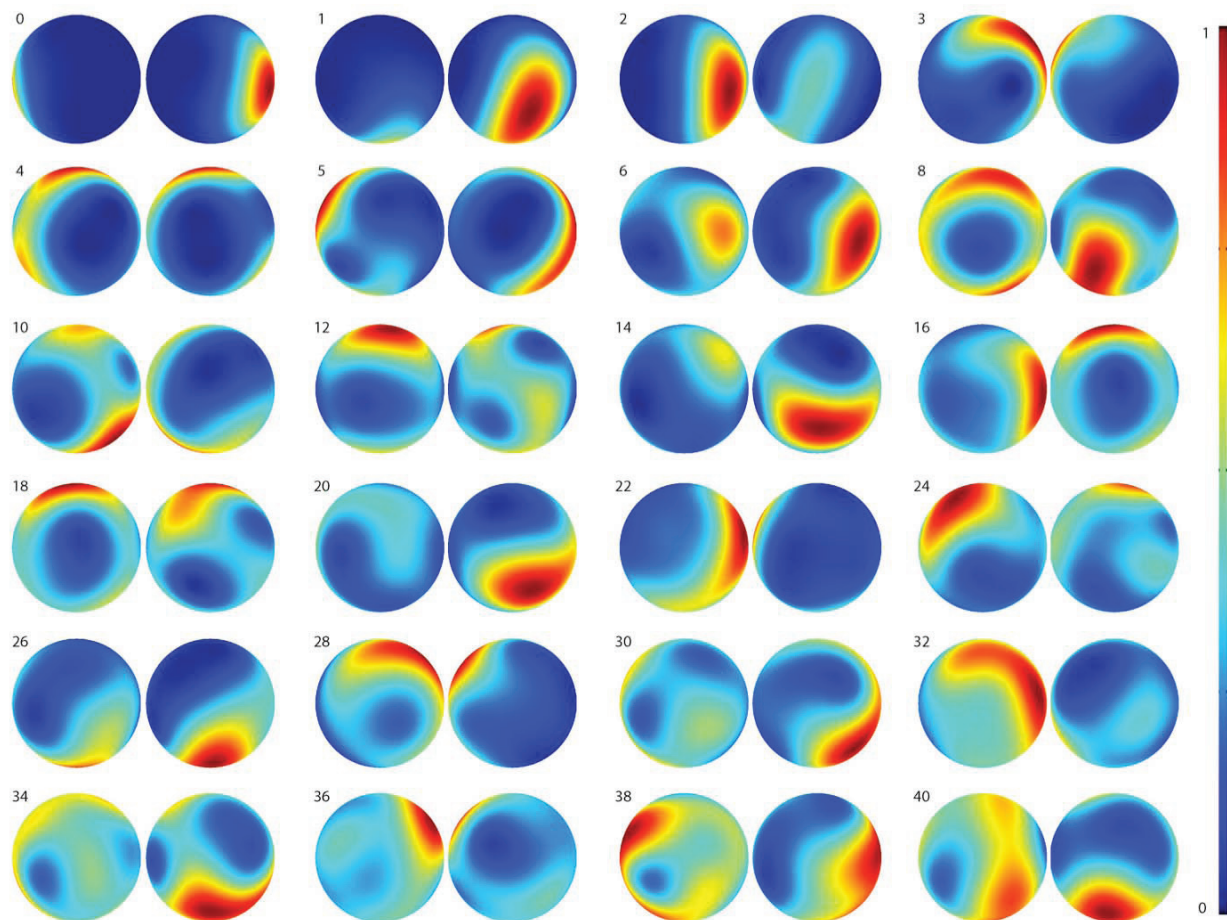
Supplementary Figure 4 | Sea of Chaos. Evolving quantum phase space (Husimi) distributions for an initial state localized in the sea of chaos in the $F_y > 0$ hemisphere. The period number is indicated to the upper left of each frame. This sequence contain our entire experimental data set, as used in the average shown in Fig. 2C, b including frames missing from Fig. 2B. Both hemispheres are shown.

Measures of dynamically generated entanglement. For a bipartite quantum system in an overall pure state entanglement between the two subsystems can be quantified by the entropy of either subsystem[9,10,11]. In our case one convenient choice is the linear entropy of the electron spin, $S_{LE} = 1 - Tr[\rho_e^2]$, which can be related to the spread of the probability distribution for the total classical spin in phase space[12]. For states in the $F = 3$ hyperfine manifold, the possible linear entropy falls in the range $0.21875 \leq S_{LE} \leq 1/2$, where the lower bound corresponds to a minimally entangled spin coherent state and the upper bound to a maximally entangled state. Supplementary Fig. 5 shows the dynamical generation of linear entropy as a function of the number of Kicked Top periods applied to the system, for the experimental parameters and initial states used in Fig. 2. For an initial state on the large island in the $F_y < 0$ hemisphere (Suppl. Fig. 5(a)), S_{LE} is nearly constant in time and has an average value only slightly above that of a minimally entangled state. For an initial state on the lower of the pair of islands in the $F_y > 0$ hemisphere (Suppl. Fig. 5(b)), S_{LE} increases rapidly during the first few Kicked Top periods. Perturbation free Schrödinger evolution predicts oscillations in S_{LE} due to dynamical tunneling. However, this behavior is washed out in our full Master Equation model, and no clear evidence is seen in the experimentally observed S_{LE} which quickly reaches a steady state value characteristic of intermediate entanglement. Finally, for an initial state in the chaotic sea (Suppl. Fig. 5(c)), S_{LE} increases rapidly to a steady state value corresponding to near-maximal entanglement, in both our experimental data and theoretical models. Overall, these data sets show clear differences in the rate and amount of

linear entropy generation for initial states in regions of classically regular and chaotic motion. The data sets are also typical for our experiment in that the linear entropy reaches its asymptotic value in ~5 periods, making the 40 period average a convenient and robust indicator of the entangling power of the dynamics.

Supplementary Figure 5 | Dynamical Generation of Linear Entropy. Linear entropy for the electron spin, $S_{LE} = 1 - Tr[\rho_e^2]$, as a function of the number of kicked top periods applied to the system. Red dots are experimental data, the dashed blue line is the prediction from perturbation free Schrödinger evolution, and the solid green line is the prediction from our full Master Equation model. The black dashed line at $S_{LE} = 0.21875$ is the minimum possible linear entropy in the $F = 3$ manifold. (a) Initial state on the large island in the $F_y < 0$ hemisphere. (b) Initial state on the lower of the pair of islands in the $F_y > 0$ hemisphere. (c) Initial state in the sea of chaos in the $F_y > 0$ hemisphere. Clear differences in the rate and amount of linear entropy generated are seen for classically regular motion in (a) and classically chaotic motion in (c). Dynamical tunneling in (b) represents an intermediate case. . Experimental error bars are plus/minus one standard deviation.

When the overall state of a bipartite quantum system is mixed the entropy of the individual subsystems is no longer a reliable indicator of entanglement between them. As evidenced by Fig. 3, this can eventually become a concern in our system. In this situation we can quantify the electron-nuclear spin entanglement with a different measure of entanglement, the negativity[13], which remains valid when the overall state is mixed. The negativity is defined as $\mathcal{N}(\rho) = (\|\rho\| - 1)/2$, where $\|\rho\|$ is the trace norm of the partial transpose of the total spin density matrix, $\|\rho\| = Tr[\sqrt{\rho^\dagger \rho}]$. Supplementary Fig. 6 shows the dynamical generation of negativity as a function of Kicked Top period. Once again there are clear differences in the rate and amount of negativity generated for initial states in classically regular versus chaotic regions, and these differences are qualitatively similar to those seen in the linear entropy. In particular, the chaotic case in Suppl. Fig. 6(c) shows a significant increase in negativity over the first

~15 Kicked Top periods. This serves as an unambiguous signature of entanglement between the electron and nuclear spins. At longer times the negativity decreases again, as outside perturbations cause the electron and nuclear spins to become correlated with their environment rather than each other. It is notable that the dual effects of electron-nuclear entanglement and overall decoherence combine to keep the linear entropy almost constant during most of the observed time window. This is not entirely surprising as both are similarly affected by the presence of chaos, though the degree to which one compensates for the other is most likely a coincidence specific to our experiment.
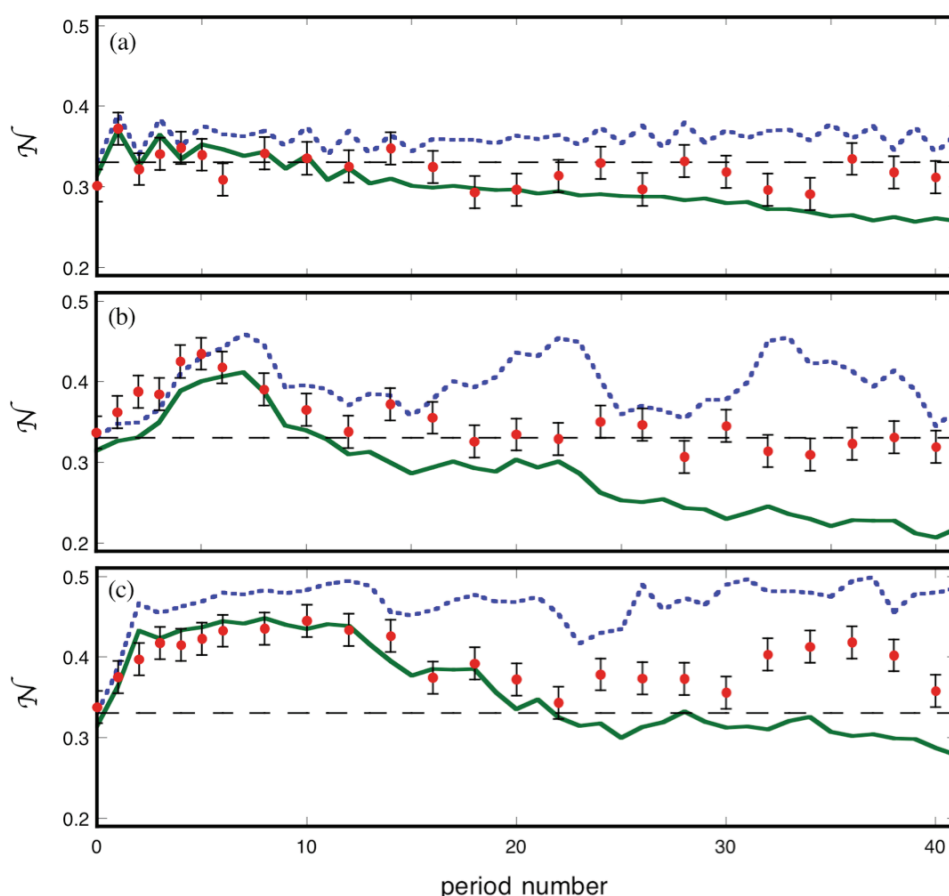
Supplementary Figure 6 | Dynamical Generation of Negativity. Negativity for the electron spin, $\mathcal{N} = (Tr[\sqrt{\rho^+\rho}]-1)/2$, as a function of the number of kicked top periods applied to the system. Red dots are experimental data, the dashed blue line is the prediction from perturbation free Schrödinger evolution, and the solid green line is the prediction from our full Master Equation model The black dashed line is the minimum possible negativity for a pure state in the $F = 3$ manifold. (a) Initial state localized on the large island in the $F_y < 0$ hemisphere. (b) Initial state localized on the lower of the pair of islands in the $F_y > 0$ hemisphere. (c) Initial state localized in the sea of chaos in the $F_y > 0$ hemisphere. Clear differences in the rate and amount of linear entropy generated is again seen for classically regular versus chaotic motion, with dynamical tunneling representing an intermediate case. As expected, the negativity drops below that of a pure state for long times due to decoherence of the overall spin state. . Experimental error bars are plus/minus one standard deviation.

Experimental Errors and Uncertainty. The primary sources of uncertainty in our experiment are errors in the experimental parameters (κ, p, and background magnetic fields), and errors in the experimental quantum state estimation. The 5% variation of κ across our atomic ensemble is carefully measured and known to be constant over time, and is built into our theoretical model. From past experience we estimate that the uncertainty in the mean κ and in p is $\leq 1\%$, and that the uncompensated background magnetic field fluctuates randomly with an amplitude of

$\sim 50\mu G$ RMS per axis. These small deviations lead to a gradual divergence between the measured Husimi distributions and those predicted by our full model. As one might expect, the discrepancies are small if the initial state lies in a regular region of phase space, but can become quite noticeable after 40 kicked top periods if the initial state lies in the sea of chaos. The parameter errors are not, however, large enough to significantly alter the structure of the Floquet states and the classical phase space, and the parts of phase space explored by the dynamics is therefore largely unaffected. This is confirmed by the time averaged Husimi distributions in Fig. 2C. A similar robustness is generally seen when we calculate the overall state purity, $Tr[\rho^2]$, or the electron spin linear entropy, $S_{LE} = 1 - Tr[\rho_e^2]$, from the measured or predicted states. The exceptions are those states that overlap significantly with the pair of islands in the $F_y > 0$ hemisphere, whose evolution due to dynamical tunneling is unusually sensitive to κ variations. This is one important contribution to the substantial difference between the predictions of our perturbation free and full models in the $F_y > 0$ region of Fig. 4b. A second contribution arises due to decoherence from photon scattering, which increases when states become delocalized in phase space. The excess sensitivity to κ variation and decoherence near the island pair will presumably be suppressed along with dynamical tunneling for a spin that is large enough to be in the semiclassical regime.

Based on past experience we estimate the typical fidelity of our quantum state reconstruction protocol to be ~90%. The precise nature of the state estimation errors is unknown, but some insight can be gained from a simple model that assumes random errors. We have simulated the effect of random errors by picking a small sample of experimentally measured states, and in each case generating an unbiased, random sample of nearby states with relative fidelity above a certain value, e. g. 80%. Our current method is too numerically inefficient to make firm quantitative predictions, but two important qualitative conclusions can be drawn. First, state reconstruction errors tend to reduce the apparent state purity, and this effect is more pronounced for nearly pure states than for mixed states. This is consistent with the behavior seen in Fig. 3, where data points with high purity tend to lie significantly below the predictions of our full model. Second, state reconstruction errors tend to increase the apparent electron spin linear entropy, and this effect is also most pronounced for nearly pure states. A good example is the state localized near the center of the large island in the $F_y < 0$ hemisphere, which remains relatively pure (Fig. 3a) and whose time average $\langle S_{LE} \rangle$ lies well above the theoretical prediction.

To complement the above error analysis, it is useful to estimate statistical uncertainty directly from experimental data sets of the type shown in Fig. 3 and Supplementary Fig. 5. The statistical uncertainty of a purity measurement can thus be estimated, either from fluctuations of the measured purity of the initial states, or from the period by period fluctuations of the measured purities relative to a smooth fit through the data. Applied across our entire data set, these two approaches suggest a standard deviation of ~10%, in addition to the systematic effects discussed above. This is the value used for error bars in Fig. 3. Applying the same method to measurements of the electron spin linear entropy, we estimate a standard deviation of ~ 0.02. This is the value used for error bars in Supplementary Fig. 5. The time average $\langle S_{LE} \rangle$ includes 24 data points, and one might hope for the uncertainty of the average to be reduced by a factor of ~ 5. In practice, by comparing a small number of available data sets for which we expect the same $\langle S_{LE} \rangle$, we find that the observed value fluctuates with a standard deviation closer to ~0.015, which suggests the presence of additional systematic errors. We have used this very conservative estimate of the standard deviation for the error bars in Fig. 4b. Error bars in Supplementary Fig. 3b and Supplementary Fig. 6 are estimated using the same methods as for Fig. 3 and Supplementary Fig. 5.

1 . Reichl, L. E. *The transition to chaos: conservative classical systems and quantum manifestations* (Springer, 2004).
2. Smith, G. A., Chaudhury, S., Silberfarb, A., Deutsch, I. H., & Jessen, P. S. Continuous Weak Measurement and Nonlinear Dynamics in a Cold Spin Ensemble. *Phys. Rev. Lett.* **93**, 163602 (2004).
3. Cohen-Tannoudji, C., Dupont-Roc, J., & Grynberg, G., *Atom-photon interactions* (Wiley, 1992).
4. Silberfarb, A., Ph.D. thesis, University of New Mexico, 2006 (unpublished).
5. Smith, G. A., Silberfarb, A., Deutsch, I. H., & Jessen, P. S. Efficient Quantum-State Estimation by Continuous Weak Measurement and Dynamical Control. *Phys. Rev. Lett.* **97**, 180403 (2006).
6. Chaudhury, S. et al. Quantum Control of the Hyperfine Spin of a Cs Atom Ensemble. *Phys. Rev. Lett.* **99**, 163002 (2007).

7.   Smith, G. A., Ph.D. thesis, University of Arizona, 2006 (unpublished).
8.   Klose, G., Smith, G., & Jessen, P. S., Measuring the Quantum State of a Large Angular Momentum. *Phys. Rev. Lett.* **86**, 4721-4724 (2001).
9.   Plenio, M. B. & Virmani, S. An introduction to entanglement measures. *Quant. Inf. Comp.* **7**, 1-51 (2007).
10. Wang, X., Ghose, S., Sanders, B. C., & Hu, B. Entanglement as a signature of quantum chaos. *Phys. Rev. E* **70**, 016217 (2004).
11. Ghose, S., & Sanders, B. C. Entanglement dynamics in chaotic systems. *Phys. Rev. A* **70**, 062315 (2004).
12. Ghose, S., Stock, R., Jessen, P., Lal, R., & Silberfarb, A. Chaos, entanglement, and decoherence in the quantum kicked top. *Phys. Rev. A* **78**, 042318 (2008).
13. Vidal, G. & Werner, R. F., Computable measures of entanglement. *Phys. Rev. A* **65**, 032314 (2002).